

# SHAPING PROTO-PLANETARY AND YOUNG PLANETARY NEBULAE WITH COLLIMATED FAST WINDS

CHIN-FEI LEE AND RAGHVENDRA SAHAI

Jet Propulsion Laboratory, MS 183-900, 4800 Oak Grove Drive, Pasadena, CA 91109

chinfei@eclipse.jpl.nasa.gov, sahai@eclipse.jpl.nasa.gov

*October 30, 2018*

## ABSTRACT

Using two-dimensional hydrodynamical simulations, we investigate the interaction of a collimated fast wind (CFW) interacting with a spherical asymptotic giant branch (AGB) wind as the mechanism for shaping proto-planetary nebulae and young planetary nebulae. In particular, we compare our simulations to the observations of an evolved PPN with multiple, highly collimated lobes, CRL 618. We characterize our model CFW by three parameters: opening angle, velocity and mass-loss rate, and explore the dependence of the properties of the shell on the first two. For given opening angle and velocity, the mass-loss rate is chosen to give a shell velocity of about  $150 \text{ km s}^{-1}$  at the tip, similar to that seen in CRL 618. In our simulations, the shell dynamics is found to depend on the velocity of the fast wind: we obtain a momentum-driven shell for a  $300 \text{ km s}^{-1}$  fast wind and a ballistic bow-shock driven shell for a  $1000 \text{ km s}^{-1}$  fast wind. The shell driven by the collimated fast wind is highly collimated, even though the AGB wind is spherical. Time variations in the velocity of the fast wind produce a series of internal shock pairs interacting with the inner surface of the shell. Due to radial expansion, the density of the internal shocks decreases with distance.

Various emission diagnostics have been derived from our simulations. For a  $300 \text{ km s}^{-1}$  fast wind, the optical emission arises from both the shocked AGB wind and shocked fast wind, showing one or two bright bow-like structures at the tip of the lobe. However, for a  $1000 \text{ km s}^{-1}$  fast wind, since the shocked fast wind is much hotter, it emits mainly in X-ray emission; the optical emission forms only one bow-like structure at the tip associated with the shocked AGB wind. The position-velocity (PV) diagrams derived from our simulations all show a broad range of velocities at the tip. The detailed PV structure and velocity range at the tip depend on the shell dynamics and the relative contributions of the shocked fast wind and shocked AGB wind.

We make a detailed comparison of our simulations to the observations of the relatively isolated north-western (W1) lobe of CRL 618. We find that a  $300 \text{ km s}^{-1}$  collimated fast wind with an opening angle of  $10^\circ$  can readily produce a highly collimated lobe similar to the W1 lobe, including the bow-like emission structure at its tip. However, our models have difficulty producing the bright emission structures seen along the body of the lobe. The  $[\text{SII}]\lambda 6716\text{\AA}/\lambda 6730\text{\AA}$  ratios at the tip of the lobe in all of our simulations are similar to that observed at the tip of the W1 lobe. The optical line ratios indicate a temperature stratification in the tip, both for the simulations and observations, however, the temperatures at the tip of the lobe in our simulations are higher than observed. The position-velocity (PV) diagrams derived from our simulations are all qualitatively consistent with the current observations. The collimated fast wind in CRL 618 is unlikely to be steady and is not radiatively driven.

*Subject headings:* stars: AGB and post-AGB — stars: winds and outflows.

## 1. INTRODUCTION

An investigation of the physical mechanism(s) responsible for the shaping of proto-planetary nebulae (PPNs) and young planetary nebulae (PNs) is crucial for understanding the mass-loss processes during the end phases of the evolution of low- and intermediate-mass stars. During the asymptotic giant branch (AGB) phase, these cool stars undergo intense mass-loss (with rate of up to  $10^{-4} \text{ M}_\odot \text{ yr}^{-1}$ ) via a dense, slow ( $\sim 10 - 20 \text{ km s}^{-1}$ ) wind (see e.g., review by Balick & Frank 2002), forming a circumstellar envelope (CSE) of dust and gas around the star. During the PN phase, the central stars (now hot white dwarfs) lose mass via fast winds at speeds of  $\sim 1000 - 2000 \text{ km s}^{-1}$  and rates of  $10^{-8}$  to  $10^{-6} \text{ M}_\odot \text{ yr}^{-1}$  (Balick & Frank 2002). The fast wind catches up with the AGB wind and drives a shocked shell through it, forming a PN. This is the so-called interacting stellar winds (ISW) model commonly

used to explain the formation of PNs (Kwok, Purton, & Fitzgerald 1978; Kahn 1983; Balick, Preston, & Icke 1987; Frank & Mellema 1994; Dwarkadas, Chevalier, & Blondin 1996; Frank 1999).

In the ISW model, the fast winds are spherical, and the AGB CSEs are assumed to have a density higher near the equator than near the pole, so that the shells driven by the fast winds expand fastest along the nebular symmetry axis. By varying the ratio of equatorial to polar density in the CSE, the ISW model is able to produce a variety of axisymmetric (e.g. elliptical or bipolar) shaped PNs (Balick, Preston, & Icke 1987; Frank & Mellema 1994).

However, recent high spatial resolution and high dynamic-range imaging of many PPNs and young PNs with the Hubble Space Telescope (HST) shows that almost all of these have highly aspherical shapes, with a significant fraction having highly collimated bipolar or multipole

lar lobes (Sahai 2001; Sahai & Trauger 1998). Examples of objects with highly collimated lobes were also known from previous ground based observations (e.g., M 2-9, M1-91, M1-16, Corradi & Schwarz 1995; Schwarz et. al. 1997). Point symmetry, rather than axisymmetry, better characterizes the geometry of the majority of these objects [striking examples are He 2-115 (Sahai & Trauger 1998), IC 4634 (Sahai et al. 2003), and He 3-1475 (Borkowski, Blondin, & Harrington 1997)]. In view of such observations, Sahai & Trauger (1998) concluded that the ISW model could not explain the shaping of PNs, and proposed that collimated fast winds operating at the beginning of the post-AGB phase were the primary mechanism for initiating the shaping of PNs.

Several nagging problems for the ISW model existed even before the HST imaging results became available. E.g., the shocked fast winds in the ISW model (without magnetic fields) did not converge to form stable, low-ionization microstructures (Icke, Balick, & Frank 1992; Frank & Mellema 1994; Dwarkadas & Balick 1998) like ansae, thin jets, or FЛИERs (Balick et al. 1993), since at the high speeds of the fast winds, most windblown bubbles are “energy conserving” (Dyson & Williams 1980). MHD models with a toroidal magnetic field embedded in a normal radiatively driven stellar wind are found to be able to produce such microstructures (Rozyczka & Franco 1996; Garcia-Segura 1997). However, the initial conditions in these models may not be appropriate (Gardiner & Frank 2001). In addition, these models require radiatively driven winds which can not account for the very large momentum excesses observed in PPNs (Bujarrabal et al. 2001). Moreover, in order to produce bipolar PNs with collimated lobes and narrow waists, very high ratios of equatorial to polar densities of the AGB winds were needed (Balick, Preston, & Icke 1987; Mellema 1995). However, less than 20% of the AGB envelopes show significant deviations from spherical symmetry (Bujarrabal & Alcolea 1991; Neri et al. 1998). Faint, roughly round halos can be seen around bright PPNs and young PNs, indicating that their progenitor AGB envelopes are produced by isotropic mass-loss (Chu, Jacoby, & Arendt 1987; Sahai 2001). The dense equatorial waist observed in many bipolar PPNs (e.g., Sahai et al. 1998; Kwok, Su, & Hrivnak 1998; Su et al. 1998) may actually result from the interaction between a collimated fast wind and the spherical AGB wind (Soker & Rappaport 2000).

Thus, the evidence for the presence of CFW’s in dying stars seems overwhelming, yet very little work has been done so far in order to investigate in detail how CFWs can shape the circumstellar environment in these objects, and to constrain the physical properties of the CFWs through quantitative comparisons with observations. This paper makes a first attempt at addressing the above lack. We explore the interaction of a CFW with a spherical AGB wind using two-dimensional hydrodynamical simulations. The CFW is assumed to emanate radially from the source with a density decreasing from the pole to the equator. It is thus structurally different from a *cylindrical* jet, which emanates along the outflow axis with constant diameter and density. Cylindrical jet models are much more common in the literature. These have been explored extensively in the case of YSOs (Blondin, Fryxell & Konigl 1990;

Stone & Norman 1994; Biro & Raga 1994; Raga et al. 1995; Suttorp et al. 1997), and to a much lesser extent, for PNs (Cliffe et al. 1995; Steffen & López 1998). A CFW model has been used to produce the bipolar lobes associated with the luminous blue variable,  $\eta$  Car (Frank, Ryu, & Davidson 1998).

We support the results of our numerical simulations by comparison with analytical outflow models, and derive observational diagnostics for comparison with observations. In §2 and 3, we describe the parameters and the numerical method used in the simulations. In §4, we present our simulations and compare them with analytical outflow models. In §5, we compare our simulations with the observations of a young PPN, CRL 618. We summarize and conclude our work in §6.

## 2. NUMERICAL SIMULATION PARAMETERS

In our simulations, the AGB wind is assumed to be spherically symmetric with the density given by (in spherical coordinate)

$$\rho_a = \frac{\dot{M}_a}{4\pi r^2 v_a} \quad (1)$$

where  $\dot{M}_a$  and  $v_a$  are the mass-loss rate and velocity of the AGB wind, respectively. For our simulations to be compared with the observations of CRL 618,  $\rho_a$  is calculated with  $\dot{M}_a = 3 \times 10^{-5} M_{\odot} \text{ yr}^{-1}$  and  $v_a = 20 \text{ km s}^{-1}$ , the values comparable to those for CRL 618 (Knapp & Morris 1985). After  $\rho_a$  is calculated, however,  $v_a$  is set to zero because it is very small compared to the velocity of the fast wind. This assumption of  $v_a$  is appropriate in this paper, because we focus on the shell dynamics away from the equatorial regions. The temperature of the AGB wind is low and set to 10 K.

At present, there is no consensus on how the fast wind is launched and collimated. One possibility is that the fast wind is launched from a magnetized accretion disk and star system by the magneto-centrifugal forces, as proposed for AGN jets (e.g., Blandford & Payne 1982) and protostellar winds/jets (e.g., Shu et al. 1994; Konigl & Pudritz 2000). These winds/jets are highly collimated by the magnetic fields. Keeping in mind our lack of understanding of the physical mechanisms driving the fast wind, we assume a *simple* parametrized description of the CFW density and velocity structure:

$$\begin{aligned} \rho_f &= \rho_{fo} \exp [-(\theta/\theta_f)^2] \\ \mathbf{v}_f &= v_{fo} \exp [-(\theta/\theta_f)^2] \hat{\mathbf{r}} \end{aligned} \quad (2)$$

where  $\rho_{fo}$  and  $v_{fo}$  are the density and velocity at the pole (where  $\theta = 0^\circ$ ), and  $\theta_f$  is the opening angle. The momentum per unit volume of the fast wind has a full width at half maximum of  $\sqrt{2 \ln 2} \theta_f = 1.18 \theta_f$ . For a given mass-loss rate of the fast wind (into two opposite sides of the central source),  $\dot{M}_f$ , the density at the pole is

$$\rho_{fo} = \frac{\dot{M}_f}{4\pi r_f^2 v_{fo} K} \quad (3)$$

where  $r_f$  is the launching radius of the fast wind and

$$K = \int_0^{\pi/2} \exp[-2(\frac{\theta}{\theta_f})^2] \sin \theta \, d\theta \quad (4)$$

In our simulations,  $\rho_{fo}$  is calculated from  $\dot{M}_f$  with  $r_f$  assumed to be  $5 \times 10^{15} \text{ cm}$  (333 AU), so that our fast wind is

characterized by three parameters:  $\dot{M}_f$ ,  $v_{fo}$  and  $\theta_f$ . Originating near or from the post-AGB star, the fast wind is assumed to have a temperature of  $10^4$  K.

The parameters of the fast wind in our simulations are listed in Table 1. Observationally, the fast wind is found to have a velocity up to  $\sim 2000$  km s $^{-1}$  (e.g., He 3-1475, Sánchez Contreras & Sahai 2001). Here,  $v_{fo}$  is set to two velocities, 300 and 1000 km s $^{-1}$ . In the simulation with  $v_{fo} = 1000$  km s $^{-1}$ ,  $v_{fo}$  is allowed to increase linearly from 0 to 1000 km s $^{-1}$  in the first 10 years to avoid a very strong shock at the beginning. As we will see later, these two velocities of  $v_{fo}$  result in qualitatively different dynamics in the simulations.  $\theta_f$  is set to  $10^\circ$  and  $20^\circ$  in order for our simulations to be compared with highly collimated PPNs and young PNs.  $\dot{M}_f$  ranges from  $2.5 \times 10^{-7}$  to  $10^{-5}$  M $_\odot$  yr $^{-1}$ . It is chosen to give a shell velocity at the tip of about 150 km s $^{-1}$ , which is comparable to that seen in CRL 618 (Sánchez Contreras, Sahai, & Gil De Paz 2002, hereafter SCSG02).

The fast wind may have periodical variations in density and velocity, as suggested in e.g., CRL 618 (SCSG02). Such variations could result from variations in the accretion process as suggested for protostellar winds (Hartmann & Kenyon 1996). In this case, the density and velocity are assumed to vary in such a way that the mass-loss rate of the fast wind is constant over the variation. Hence, the fast wind is assumed to have

$$\begin{aligned}\rho'_f &= \rho_f / (1 + A \sin \frac{2\pi t}{P}) \\ \mathbf{v}'_f &= \mathbf{v}_f (1 + A \sin \frac{2\pi t}{P})\end{aligned}\quad (5)$$

where  $A$  and  $P$  are the amplitude and period of the variation. Such variations in density and velocity have also been used in simulations of protostellar winds/jets in order to produce knotty and bow-like structures along the outflow axis (see e.g., Biro & Raga 1994; Lee et al. 2001).

### 3. EQUATIONS AND NUMERICAL METHOD

The two-dimensional hydrodynamic code, ZEUS 2D, is used to solve the equations of hydrodynamics,

$$\begin{aligned}\frac{\partial \rho}{\partial t} + \nabla \cdot (\rho \mathbf{v}) &= 0 \\ \frac{\partial \rho \mathbf{v}}{\partial t} + \nabla \cdot (\rho \mathbf{v} \mathbf{v}) &= -\nabla p + f \\ \frac{\partial e}{\partial t} + \nabla \cdot (e \mathbf{v}) &= -p \nabla \cdot \mathbf{v} - n^2 \Lambda\end{aligned}\quad (6)$$

where  $\rho$ ,  $\mathbf{v}$ ,  $p$ ,  $e$ , and  $n$  are the mass density, velocity, thermal pressure, internal energy density, and hydrogen nuclei number density, respectively. An ideal gas equation of state  $p = (\gamma - 1)e$  with  $\gamma = 5/3$  is used for the thermal pressure. Helium is included as a neutral component with  $n(\text{He}) = 0.1 \cdot n$ , so that  $n = \rho / (1.4 \cdot m_H)$ , where  $m_H$  is the mass of atomic hydrogen. In our simulations, the undisturbed AGB wind is assumed to be static. As a result, a small fixed force per unit volume,  $f$ , is introduced in our simulations to hold the undisturbed AGB wind from thermal expansion. Here  $f = -\frac{2p_a}{r}$ , where  $p_a$  is the thermal pressure of the undisturbed AGB wind.  $\Lambda$  is the optically thin radiative cooling function for interstellar gas, with the function at high temperature from

MacDonald & Bailey (1981) and the function at low temperature from Dalgarno & McCray (1972). We assume an equilibrium cooling function, in which the ionization fraction of hydrogen is calculated by equating the ionization rate with the recombination rate of hydrogen. As a result, the cooling function decreases rapidly at about  $10^4$  K as the ionization fraction of hydrogen decreases. Molecular cooling is not included.

Scalar tracers,  $c$ ,  $c_a$ , and  $c_w$ , are also included in the simulations to track the fast and AGB winds.  $c$  tracks the fast wind, it is one for the fast wind, zero for the AGB wind, and a value between one and zero for a mixture of the fast wind and AGB wind.  $c_a$  and  $c_w$  trace respectively the flows of the AGB wind and the fast wind in the strongly interacting regions near the pole. Thus,  $c_a$  ( $c_w$ ) is one for the AGB (fast) wind emanating within the angular segment  $5^\circ < \theta < 7.5^\circ$ , a value between one and zero for a mixture of this material with the rest, and zero for the rest.

Simulations are performed in spherical coordinates with a computational domain of dimensions  $(r, \theta) = (5 \times 10^{15} \text{ to } 10^{17} \text{ cm}, 0 \text{ to } \theta_b)$  and a uniform grid of  $400 \times 400$  zones. This gives a resolution of  $2.37 \times 10^{14}$  cm in  $r$ .  $\theta_b$  is a value between 0.5 and  $\pi/2$  depending on the angular extent of the simulations, giving a resolution of  $1.25 \times 10^{-3}$  to  $4 \times 10^{-3}$  radians in  $\theta$ . Reflecting boundary conditions are used along the inner  $\theta$  (where  $\theta = 0^\circ$ ) and outer  $\theta$  (where  $\theta = \theta_b$ ) boundaries, while outflow boundary conditions are used along the outer  $r$  boundary. Inflow boundary conditions are used for inner  $r$  boundary to introduce the fast wind into the AGB wind. The results of the simulations are presented in cylindrical coordinates (z,R), with the z-axis being the outflow axis.

## 4. RESULTS

In this section, we present the results of our simulations as the fast wind propagates to a distance of about  $10^{17}$  cm, a length similar to that of the lobes in CRL 618. Observationally, a significant amount of optical emission is believed to come from a shell surrounding the fast wind, therefore, we concentrate on the shell dynamics in the simulations. Model 1 is considered as a standard model because it can produce a shell with a collimation similar to that of CRL 618. We discuss the effects of changing the opening angle and velocity of the fast wind on the structure and kinematics of the shell. We use analytical models to support the results of our simulations. At the end of this section, we discuss how the velocity of the fast wind changes the shell dynamics in the simulations.

### 4.1. Model 1: Standard model

The simulation of model 1 is presented in Figure 1. The fast wind is 177 years old. In this model,  $\dot{M}_f = 2.5 \times 10^{-6}$  M $_\odot$  yr $^{-1}$ ,  $v_{fo} = 300$  km s $^{-1}$ , and  $\theta_f = 10^\circ$ . As the fast wind blows into the AGB wind, a shell is formed around the fast wind. The shell is highly collimated with a length to width ratio of about 6. It consists of shocked AGB wind (forward shock) and shocked fast wind (backward shock) separated by a contact discontinuity (mixture), as indicated by the  $c$  contours. Since the heat generated by the fast wind's kinetic energy is efficiently converted into escaping radiation, the shocked fast wind becomes a thin

inner shell accelerating the shocked AGB wind in the outer shell. As a result, the shell is a “momentum-conserving” wind-driven shell. The motions of the shocked fast wind and shocked AGB wind are different. The shocked fast wind moves along the shell toward the pole, producing a focusing effect that in turn produces a high-density jet-like structure at the tip, as indicated by the  $c_w$  contours (see Canto, Tenorio-Tagle, & Rozyczka 1988; Frank, Balick, & Livio 1996b). The detailed structure of the jet-like structure, however, depends on the numerical resolution. The shocked AGB wind moves along the shell toward the equator, as indicated by the  $c_a$  contours. This motion of the shocked AGB wind depends on the relative velocity between the shell and undisturbed AGB wind and thus will still be important even if the undisturbed AGB wind has a radial expansion of  $20 \text{ km s}^{-1}$ . However, this motion is not able to produce mass accumulation at the equator due to high density (thus inertia) of the shell material near the equator. In the simulation, no Kelvin-Helmholtz instability is seen along the contact discontinuity because the velocity changes smoothly within the shell and the resolution in our simulation is low. The velocity decreases from the shocked fast wind in the inner shell to the shocked AGB wind in the outer shell, indicating that the momentum of the shocked fast wind is not transferred immediately to the shocked AGB wind due to the thermal pressure in the shell. The shell velocity,  $v_s$ , decreases with latitude from the pole to the equator but increases with time. The velocity at the tip where  $\theta = 0^\circ$  is found to be  $v_{so} = 138(1 + 0.00165t_{yr}) \text{ km s}^{-1}$ , where  $t_{yr}$  is the outflow age of the fast wind in units of years. At the age of 177 years,  $v_{so}$  is  $178 \text{ km s}^{-1}$ .

The fast wind itself cools rapidly as it propagates away from the source due to adiabatic expansion and radiative cooling. For the temperature of the fast wind,  $T_f$ , we have

$$\frac{dT_f}{dr} = -\frac{4}{3} \frac{T_f}{r} - \frac{2n\Lambda}{3kv_f} \quad (7)$$

Due to radial expansion, the number density  $n = \frac{\rho_f}{1.4m_H} \left(\frac{r_f}{r}\right)^2$ . Thus,

$$\frac{dT_f}{dr} = -\frac{4}{3} \frac{T_f}{r} - \frac{\rho_f \Lambda}{2.1m_H k v_f} \left(\frac{r_f}{r}\right)^2 \quad (8)$$

Integrating this equation numerically, we find that the fast wind cools down from  $10^4$  to  $10^2 \text{ K}$  after traveling a distance of  $1.2 \times 10^{16} \text{ cm}$  from the source, consistent with the simulation. The majority of the shell has a temperature of about  $10^4 \text{ K}$  at which the cooling function decreases rapidly (see §3). The temperature of the shell is highest at the shell boundaries near the pole where the material is recently and strongly shocked, about  $10^5 \text{ K}$  for the shocked AGB wind and a few  $10^4 \text{ K}$  for the shocked fast wind. The temperature decreases away from the pole as the shell velocity decreases. The temperature also depends on the radiative cooling and thus the density. Near the source where the density is high, the shocked AGB wind cools to less than  $100 \text{ K}$  (due to the cooling of atomic gas at low temperature in our cooling function, see Dalgarno & McCray 1972). The dense jet-like structure at the tip also cools to a very low temperature compared to its surrounding shell material.

In order to further investigate the shell dynamics, we present the transverse velocity,  $v_R$ , and longitudinal velocity,  $v_z$ , of the shell material in Figure 2. The velocity

structures of the newly shocked fast wind and the newly shocked AGB wind are different. The transverse velocity of the newly shocked fast wind decreases with increasing  $z$ . It becomes negative near the pole but drops rapidly to zero at the tip, indicating that the newly shocked fast wind is focused toward the pole and shocked strongly at the tip. At the tip, the sound speed of the newly shocked fast wind,  $c_s$ , is  $12 \text{ km s}^{-1}$ . According to Bernoulli’s theorem, the transverse velocity of the newly shocked fast wind is limited to  $\sqrt{3}c_s$  or  $20 \text{ km s}^{-1}$  for  $\gamma = 5/3$ . On the other hand, as we go from the tip to the central source (decreasing  $z$ ), the transverse velocity of the newly shocked AGB wind first shows a rapid increase in the tip (indicating that the newly shocked AGB wind at the tip is squirted sideways along the shell) and then shows a steady linear decrease. Since the momentum of the fast wind is mainly along the  $z$ -axis, the longitudinal velocity of the newly shocked AGB wind is very low except near the tip.

In the following, we compare the shell structure and kinematics in the simulation of model 1 to a simple analytical momentum-driven shell model given by Lee et al. (2001), which was found to be able to describe the shell dynamics in similar but isothermal wind simulations. In this analytical model, the thermal pressure in the shell and the motion of the shocked fast and AGB winds along the shell are not considered. In this case, the ram pressure of the fast wind is exactly balanced by that of the AGB wind, so that the shell expands outward with a constant velocity along any radial direction. Hence, the shell velocity (see Figure 3) is,

$$\mathbf{v}_s(\theta) = \frac{\mathbf{v}_f(\theta)}{1 + \eta^{-1/2}} \quad (9)$$

and the shell radius is

$$r_s(\theta) = v_s(\theta)t + r_f \quad (10)$$

where  $\eta \equiv \frac{r_f^2 \rho_f}{r^2 \rho_a} = \frac{1}{K} \frac{M_f}{M_a} \frac{v_a}{v_f}$ . Therefore, the shell velocity at the tip,  $v_{so}$ , is expected to be  $138 \text{ km s}^{-1}$ , in agreement with the initial shell velocity as the fast wind first impacts the AGB wind in the simulation. However, in the simulation, the shell velocity increases with time as the shocked fast and AGB winds flow along the shell. As a result, the predicted shell structure (the dashed line in Figure 1a) is smaller than that in the simulation.

The velocity of the newly shocked fast wind can be derived from the shell velocity. However, since the shell velocity increases with time in the simulation, a mean (averaged over time) shell velocity,  $\bar{v}_s$ , is used to derive the velocity of the newly shocked fast wind. The mean shell velocity is  $\bar{v}_s(\theta) = (r_s(\theta) - r_f)/t$ . As expected, its  $R$  and  $z$  components (the solid lines in Figure 2) lie between those of the newly shocked fast wind and the newly shocked AGB wind. The velocity of the newly shocked fast wind is

$$\mathbf{v}_{sf} = \mathbf{v}_f - \frac{2(v_f - \bar{v}_s)}{\gamma + 1} \cos \alpha [\sin(\alpha + \theta) \hat{\mathbf{R}} + \cos(\alpha + \theta) \hat{\mathbf{z}}] \quad (11)$$

where  $\alpha$  is the angle between the shell normal and the mean shell velocity (see Figure 3) – note that the dependence of various parameters on  $\theta$  is not explicitly shown in the equation. Its  $R$  and  $z$  components (the dashed lines in Figure 2) are found to match reasonably well those of the

newly shocked fast wind in the simulation, except near the tip where the shocked fast wind shocks with itself, producing a thermal pressure gradient that reduces the transverse velocity near the tip. With this equation, the transverse velocity of the newly shocked fast wind is found to become negative as  $\theta < \theta_c$ , where

$$\sin \theta_c = \frac{2(v_f - \bar{v}_s)}{v_f(\gamma + 1)} \cos \alpha \sin(\alpha + \theta_c) \quad (12)$$

As a result, the shocked fast wind with  $\theta < \theta_c$  or  $3.4^\circ$  is focused toward the pole, producing a focusing effect that produces a shell longer than the momentum-driven shell in the simple analytical model.

#### 4.2. Model 2: Effects of changing the opening angle

The effects of the opening angle of the fast wind can be studied by comparing the simulation of model 2 to that of model 1. The simulation of model 2 is presented in Figure 4. The age is 188 years. In this model,  $\dot{M}_f = 1 \times 10^{-5} M_\odot \text{ yr}^{-1}$ ,  $v_{fo} = 300 \text{ km s}^{-1}$ , and  $\theta_f = 20^\circ$ . The mass-loss rate is adjusted to give the same  $\rho_{fo}$  and thus the same initial shell velocity at the tip as model 1 (see Equation 9). The shell dynamics in this model is qualitatively the same as that of model 1. However, driven by a fast wind with twice opening angle, the shell has a length to width ratio of about 3, half of that in model 1. Hence, under our assumption of the fast wind, the collimation (length to width ratio) of the shell increases roughly linearly with decreasing opening angle of the fast wind. In addition, since the shell velocity decreases slower away from the pole, the temperature at the shell boundaries also decreases slower away from the pole. Moreover, since the angle between the shell normal and the shell velocity is everywhere smaller, the focusing effect of the shocked fast wind is less. As a result, the shell velocity increases with time slower than that of model 1, so that the shell structure can be described by the simple momentum-driven shell model (see the dashed line in Figure 4a). The shell velocity at the tip is found to be  $v_{so} = 138(1 + 0.0004t_{yr}) \text{ km s}^{-1}$ , or  $148 \text{ km s}^{-1}$  at the age of 188 years.

#### 4.3. Model 3: Effects of changing the velocity

The effects of the velocity of the fast wind can be studied by comparing the simulation of model 3 to that of model 1. The simulation of model 3 is presented in Figure 5. The age is 180 years. In this model,  $\dot{M}_f = 2.5 \times 10^{-7} M_\odot \text{ yr}^{-1}$ ,  $v_{fo} = 1000 \text{ km s}^{-1}$ , and  $\theta_f = 10^\circ$ . The mass-loss rate is chosen to give an initial shell velocity of about  $150 \text{ km s}^{-1}$  at the tip, similar to that of model 1 (see Equation 9). Although the opening angle of the fast wind is the same, the shell is broader than that of model 1. Unlike model 1, the shell is mainly composed of the shocked AGB wind, as indicated by the  $c$  contours. The shocked fast wind does not cool fast enough and expands into a low-density but hot, high-pressure and turbulent cocoon surrounding the unshocked fast wind, as indicated by the  $c_w$  contours. Being compressed by this high-pressure cocoon, the fast wind itself becomes a ripple jet surrounded by a dense sheath of compressed fast wind, similar to that seen by e.g., Frank & Mellema (1996a). The jet interacts with the AGB wind, producing a rippled shell with a convex curvature at the tip. The shocked AGB wind in the

convex curvature moves toward the symmetry axis. However, since the shocked AGB wind cannot flow across the symmetry axis in the simulation, some of it is deflected in a backward direction toward the source, producing a linear and dense structure along the axis inside the shell, as seen in other simulations (Blondin & Lundqvist 1993; Dwarkadas & Balick 1998). As a result, this linear and dense structure is likely an artifact produced by the numerical effect of the simulation. Since the fast wind itself is compressed by the shocked fast wind and bent toward the  $z$ -axis, the density of the fast wind does not decrease with distance as fast as the density of the AGB wind, so that the shell velocity at the tip increases with time. At the tip, the shell velocity is about  $220 \text{ km s}^{-1}$  and the temperature of the shell is about  $10^6 \text{ K}$ , much higher than that in model 1. On the other hand, the temperature of the shocked fast wind is a few  $\times 10^7 \text{ K}$  at the head of the fast wind and decreases to a few  $\times 10^6 \text{ K}$  as the shocked fast wind expands into the cocoon. Since the shocked fast wind expands sideways at the head, there is no focusing effect in this simulation.

The transverse velocity,  $v_R$ , and longitudinal velocity,  $v_z$ , of the shell material are presented in Figure 6. Since we are interested in the shell dynamics, the shocked fast wind in the cocoon is excluded in this figure. The negative  $v_R$  is associated with the convex curvature at the tip. To avoid confusion, the convex curvature is not included in the figure of  $v_z$ . Unlike model 1, the transverse and longitudinal velocities both show a convex spur structure with the highest velocity at the tip, indicating that the shocked AGB wind at the tip, due to its high thermal pressure and the thermal expansion of the shocked fast wind at the head, is squirted sideways along the shell. This is similar to that seen in the simulations of a cylindrical jet (see e.g., Lee et al. 2001).

In the following, we compare the shell structure and kinematics in the simulation of model 3 to a simple analytical ballistic bow shock model in Ostriker et al. (2001), which was found to be able to describe the shell dynamics in the simulations of a cylindrical jet. In the ballistic bow shock model, the shocked AGB wind in the shell is assumed to be accelerated by an initial impulse at the head – the thermal pressure forces of the shocked fast wind and shocked AGB wind are ignored subsequent to the initial impulse. At the tip, the shell velocity,  $v_{so}$ , is about  $220 \text{ km s}^{-1}$  and the sound speed is about  $65 \text{ km s}^{-1}$  in the simulation. Therefore,  $v_R$  is limited to the smaller value of  $\sqrt{3}c_s$  and  $v_{so}/2$ , or  $110 \text{ km s}^{-1}$ , consistent with the ballistic bow shock model. Using Equations 18-22 in Ostriker et al. (2001) and assuming a mean jet radius of  $R_j = 4 \times 10^{15} \text{ cm}$  for the ripple jet (see Figure 5) and  $\beta = 4$  (a typical value used for the initial impulse at the head, see Lee et al. 2001; Ostriker et al. 2001), we calculated the shape of the shell (the dashed line in Figure 5), the mean shell velocity averaged over the shell thickness (the solid lines in Figure 6), and the immediate postshock velocity of the AGB wind (the dashed lines in Figure 6). As can be seen, the shape and the transverse velocity of the shell in the simulation can be reasonably reproduced with the ballistic bow shock model. However, the simple ballistic bow shock model cannot reproduce the longitudinal velocity that well. In the simulation, the material in

the shell consists of two components, one with a velocity close to the immediate postshock velocity and the other with a velocity close to the mean shell velocity.

#### 4.4. Model 4: Effects of the time variations

The effects of the time variation of the fast wind can be studied by comparing the simulation of model 4 to that of model 1. The simulation of model 4 is presented in Figure 7. The age is 166 years. In this model, the fast wind has the same parameters as that in model 1 but has a time variation in the density and velocity with  $A = 0.5$  and  $P = 22$  years (see Equation 5). The structure and velocity of the shell in this model are similar to those of model 1. There is also a jet-like structure at the tip. Inside the shell, however, there are periodic internal shock pairs (i.e. forward and backward shocks), which are clearly seen in the temperature distribution, propagating away from the source at the velocity  $v_f$ . The wings of the internal shocks grow with time and eventually impact the inner surface of the shell. The curvature of the internal shocks are determined by the angular distribution of the fast wind's velocity and thus well described by (dashed lines in Fig. 7a)

$$r(\theta) = v_f(\theta)t_i + r_f \quad (13)$$

where  $t_i$  is the age of each internal shock. The thickness of the internal shock pairs (i.e. the separation between the forward and backward shocks) increases with the distance due to thermal expansion. The thickness along the  $z$ -axis ( $\theta = 0^\circ$ ) is found to be

$$\tau = 190 + \frac{c_s}{v_f}(z - r_f) \text{ AU} \quad (14)$$

where  $c_s = 11 \text{ km s}^{-1}$ , the sound speed at the shock boundaries in the simulation. The density of the internal shocks decreases with the distance due to radial expansion. The shocked fast wind also moves along the internal shock surfaces, as indicated by the  $c_w$  contours. The leading and the internal shocks all show highest temperature at the boundaries where the material is newly shocked.

#### 4.5. Shell dynamics

It is clear that the velocity of the fast wind is a crucial parameter in determining the shell dynamics, e.g., whether the shell is momentum-driven or driven by thermal pressure. This was recognized by Dwarkadas & Balick (1998) who carried out simulations of an ISW model in which the fast wind velocity ramped up from 25 to 1000 km  $\text{s}^{-1}$  – their simulated nebulae evolve through an initial momentum-conserving phase before entering the energy-conserving stage. In our simulations, the parameters are chosen to give a shell velocity of about 150 km  $\text{s}^{-1}$  at the tip, comparable to that seen in CRL 618. For a given shell velocity at the tip,  $v_{so}$ , the velocities of the shocked AGB wind and shocked fast wind at the tip are  $v_{so}$  and  $v_{fo} - v_{so} \equiv v_{sfo}$ , respectively. In order to balance the ram pressures of the shocked fast wind and shocked AGB wind at the tip, the density of the fast wind along the  $z$ -axis ( $\theta = 0^\circ$ ) is required to be

$$\rho_{fo} = \frac{\dot{M}_a}{4\pi r_f^2 v_a} \left( \frac{v_{so}}{v_{sfo}} \right)^2 \quad (15)$$

giving a kinetic energy injection rate along the  $z$ -axis of

$$L_{ko} = \frac{K}{2} \frac{\dot{M}_a v_{fo}^3}{v_a} \left( \frac{v_{so}}{v_{sfo}} \right)^2 \quad (16)$$

For a 300 km  $\text{s}^{-1}$  fast wind, the shocked AGB wind and shocked fast wind both have a velocity of about 150 km  $\text{s}^{-1}$  at the tip. The cooling is fast enough to remove the heat obtained from the fast wind, so that the shell is thin and momentum-driven. For a 1000 km  $\text{s}^{-1}$  fast wind, however, the shocked fast wind has a velocity of 850 km  $\text{s}^{-1}$  at the tip. Thus, the fast wind is required to be more tenuous than that of 300 km  $\text{s}^{-1}$  fast wind (see Eq. 15). However, the energy injection rate is about the same (see Eq. 16), so that the shocked fast wind does not cool fast enough and expands into a hot cocoon. The fast wind itself becomes a ripple jet surrounded by a dense sheath of compressed fast wind. As a result, the shell is essentially driven by a jet. At a velocity of about 150 km  $\text{s}^{-1}$ , the shell is radiative and its kinematics can be described by a ballistic bow shock model.

#### 4.6. Comparison with previous analytical models

Recently, Soker (2002) has also developed analytical models of highly CFWs in order to reproduce highly collimated shells in PPNs and PNs. He defines two cases: (i) the “slow-propagating” jet, in which the shell at the tip proceeds at a speed  $v_{so} \ll v_{fo}$ , which can be compared to our simulations of model 3; and (ii) the “fast-propagating” jet, in which  $v_{so} \sim v_{fo}$ . In case (ii), the density of the gas in the jet is much larger than that of the AGB wind; this condition is not met in any of our simulations. In Soker's case (i) above, the shocked fast wind is assumed to be adiabatic and expands sideways behind the shell of the shocked AGB wind, similar to that seen in our simulation of model 3. He also assumes that the shell is continuously accelerated by the thermal pressure force of the shocked fast wind and expands laterally perpendicular to the outflow axis. In our simulation, however, the ram pressure in the shell is much greater than the thermal pressure of the shocked fast wind except at the head. As a result, the force due to the thermal pressure of the shocked fast wind can be ignored subsequent to an initial impulse at the head, so that the shell dynamics is in the ballistic limit. In addition, unlike his model, the shell in our simulation also expands significantly in the  $z$  direction (see Figure 6) as the momentum of the fast wind is transferred to the shocked AGB wind. As a result, his model predicts a lobe much wider than that in our simulation (model 3).

## 5. COMPARISON WITH OBSERVATIONS

In the following, we compare our simulations to the observations of CRL 618. CRL 618 is a young PPN located at a distance of 0.9 kpc (Goodrich 1991). It shows several narrow lobes at different orientations in HST images (Trammell 2000), perhaps resulting from multiple ejections at different orientations. The general structures of the different lobes are similar. We compare our simulations to the northwestern (W1) lobe, which is separated from other lobes and shows clear position-velocity diagrams in the groundbased observations. This lobe has an inclination of about 30° into the plane of the sky (SCSG02) and a length of about  $10^{17}$  cm. Since molecular cooling is not

included in our simulations, we only compare the optical emission. In the simulations, the emission is assumed to be optically thin and arising from gas in local thermal equilibrium (LTE) (see Appendix). We assume a distance of 1 kpc and an inclination of 30°, the values similar to those of CRL 618.

### 5.1. Morphology

The W1 lobe of CRL 618 is highly collimated with a length to width ratio of about 7. In optical emission, several bow-like (or ripple-like) structures are seen within the body of the lobe (see Figure 8). The  $[\text{SII}]\lambda 6716\text{\AA}/\lambda 6730\text{\AA}$  ratio is about 0.5 and roughly constant in the lobe (SCSG02). We compare our simulations to these features in order to determine which model can better produce the morphology of the lobe.

With a highly collimated fast wind, model 1 is able to produce a narrow lobe similar to the W1 lobe. In this model, the velocity of the shocked AGB wind is higher than that of the shocked fast wind, so that the optical emission arises mostly from the newly and strongly shocked AGB wind, showing a single bow-like structure at the tip (see Fig. 9). From [OIII] to [NII] to [SII] to [OI], the emission traces the material at lower and lower temperature, showing more and more extended bow-like emission structure. At the tip, the electron density is about  $10^4 \text{ cm}^{-3}$  and the  $[\text{SII}]\lambda 6716\text{\AA}/\lambda 6730\text{\AA}$  ratio is about 0.5, similar to that seen in the W1 lobe. The emission from the newly shocked fast wind could be as strong as that from the newly shocked AGB wind, showing two bow-like structures at the tip, as that seen in model 2 (see Fig. 10), in which the velocities of the shocked AGB wind and shocked fast wind happen to be comparable, about  $150 \text{ km s}^{-1}$ . Due to its high density, the material between the two bow-like structures cools down quickly and radiates very weakly in optical emission. As a result, a  $300 \text{ km s}^{-1}$  fast wind with a small opening angle can produce one or two close bow-like structures at the tip similar to that seen in the W1 lobe, however, it has difficulty producing other bow-like structures in the W1 lobe.

On the other hand, a model with a  $1000 \text{ km s}^{-1}$  fast wind has difficulty producing a narrow lobe similar to that of the W1 lobe. Although it has the same opening angle of the fast wind as that in model 1, model 3 produces a lobe much broader than the W1 lobe. We have performed a simulation using a fast wind with an opening angle half of that in model 3 but with the same velocity and density along the axis, however, the lobe in that simulation is only 15 percent smaller than that of model 3, and thus still much broader than the W1 lobe. As a result, due to thermal expansion of the shocked fast wind, the collimation of the lobe produced by a high speed fast wind increases slowly with decreasing opening angle of the fast wind. In model 3, the optical emission shows a bright bow-like structure at the tip (see Fig. 11). The emission becomes weak away from the tip. Except near the tip, the [OIII] emission is from the inner shell while the [OI] emission is from the outer shell. The  $[\text{SII}]\lambda 6716\text{\AA}/\lambda 6730\text{\AA}$  ratio is everywhere about 0.5, similar to that seen in the W1 lobe. There are ring-like emission structures arising from the ripple in the shell in the simulation (see Figure 5). However, these ring-like structures are much more

rounded than the observed bow-like structures in the W1 lobe, suggesting that the bow-like structures are not associated with the ripple in the shell. There is also a cone-like structure along the axis associated with the dense sheath of compressed fast wind around the jet (see Fig. 5). Since this structure is not seen in the W1 lobe, the hot and high-pressure cocoon that produces the dense sheath of compressed fast wind is probably not present in the W1 lobe. As a result, we conclude that the velocity of the shocked fast wind in the W1 lobe is probably smaller than that in model 3. Since the hot and high-pressure cocoon radiates in X-ray emission, future X-ray observations will be able to check the existence of the hot cocoon in the W1 lobe. For future comparison, we present the X-ray emission and spectrum in the 0.2 -1.5 keV energy range derived from model 3 in Figure 12. The total X-ray luminosity is  $L_x = 1.5 \times 10^{29} \text{ ergs s}^{-1}$ . The X-ray is strongest at the head where the shock is the strongest. There are strong emission lines from oxygen and iron in the spectrum. Current upper limits on the X-ray flux from CRL618 are roughly a factor 10 larger than our model flux. CRL618 was not detected in a 18697 sec observation with the HRI instrument onboard ROSAT (Guerrero, Chu, & Gruendl 2000). If we assume that a minimum of 9 photons are required for a  $3\sigma$  detection, we can use the detection of BD+30°3639 with HRI (172+/-13 counts in 8740 sec, Leahy et al 1998) and its measured X-ray flux  $5.7 \times 10^{-13} \text{ erg cm}^{-2} \text{ s}^{-1}$  to put a roughly upper limit on the X-ray flux of CRL618 of  $<1.4 \times 10^{-14} \text{ erg cm}^{-2} \text{ s}^{-1}$  ( $1.7 \times 10^{30} \text{ erg s}^{-1}$ ).

The series of optical bow-like structures observed in the body of the W1 lobe (as well as other lobes) but not reproduced in the previous models, suggest that the fast wind may have time variations in density and velocity. With an episodic fast wind, model 4 produces a series of optical bow-like structures in the body of the lobe (see Fig. 13). The two bright bow-like structures ( $B_1$  and  $B_2$ ) at the tip trace the newly shocked AGB wind in the outer shell and the newly shocked fast wind in the inner shell impacted by the internal shocks. However, in contrast to the observations that show a series of bow-like structures of similar intensity within the lobe, the optical emission of our model internal bow-like structures becomes progressively weaker away from the source (due to radial expansion and radiative cooling). The results for the  $[\text{SII}]\lambda 6716\text{\AA}/\lambda 6730\text{\AA}$  ratio are also inconsistent with the observations of the W1 lobe, which show a roughly constant value of 0.5 with fluctuations from 0.4 to 0.6. In our model, this ratio is (a) about 1.5 for the shell along the body of the lobe, (b) 0.6 in the bow-like structure near the source (and increases away from the source). Although there is also emission from the inner shell (that is impacted by the wings of the internal shocks), this emission does not have the observed bow-shaped geometry.

One way to resolve the above discrepancies between our model 4 and the observations is to have a mass-loss rate of the fast wind ( $\dot{M}_f$ ) that decreases with time. However, in order to produce adequate optical emission along the body of the lobe,  $\dot{M}_f$  at time  $t = 0$  would have to be a factor of  $\sim 10$  larger. Another possibility is for the underlying driving agent to be an episodic *cylindrical* jet, which has a density constant with the distance. Simula-

tions with episodic cylindrical jets have been performed by a number of authors in order to reproduce the morphology and kinematics of protostellar outflows (Stone & Norman 1993b; Raga & Cabrit 1993; Biro & Raga 1994; Suttner et al. 1997; Lee et al. 2001). Such jets can also produce a series of internal bow-like structures along the body of the lobe. Without radial expansion, the emission of these structures does not decrease as fast as that in model 4. In addition, each of these structures has overall stronger emission than its counterpart in our model 4 because it closes back to, and is shocked by, the one behind it (see Fig. 6 and 7 in Biro & Raga 1994).

### 5.2. Kinematics

The position-velocity (PV) diagrams of optical emission for cuts along the axis of the W1 lobe show a nonlinear increase in velocity with increasing distance from the source and a broad range of velocities at the tip with a FWZI up to  $200 \text{ km s}^{-1}$  (SCSG02). In this section, we present the PV diagrams of the  $[\text{OI}]\lambda 6300$  emission, the most extended emission, derived from our simulations and compare them to that of the W1 lobe. The diagrams are also degraded to low resolutions for comparing with the current observations.

The PV diagrams derived from the simulation of model 1 are presented in Figure 14. At an inclination  $i = 30^\circ$ , the newly shocked fast wind is projected at a velocity higher than that of the newly shocked AGB wind. At low resolution, the diagram shows two elliptical structures attached together. These diagrams show a broad range of velocities at the tip, qualitatively consistent with that seen in the W1 lobe. However, since the emission is mostly from the newly shocked AGB wind, the velocity range is about  $v_{so} \sin i = 89 \text{ km s}^{-1}$ , much smaller than that seen in the W1 lobe. In order to produce the observed velocity range, the shock velocity at the tip would have to be  $400 \text{ km s}^{-1}$ , resulting in a very high temperature for the shell ( $> 10^6 \text{ K}$ ). As mentioned, the emission from the newly shocked fast wind could be as strong as that from the newly shocked AGB wind. In that case, the detailed PV structure would be similar to that of model 2 (see Fig. 15) and the velocity range at the tip would be about  $v_f \sin i = 150 \text{ km s}^{-1}$ , similar to that seen in the W1 lobe.

The PV diagrams for model 3 are presented in Figure 16. They show a convex spur structure on the redshifted side, i.e., a nonlinear increase in velocity toward the tip with increasing distance from the source. There is also emission on the blueshifted side. A broad range of velocities is also seen at the tip. The maximum redshifted velocity is  $v_{so} - \frac{v_{so}}{2} \sin i = 165 \text{ km s}^{-1}$  while the maximum blueshifted velocity is  $-\frac{v_{so}}{2} \sin i = -55 \text{ km s}^{-1}$ , so that the velocity range at the tip is equal to the shock velocity at the tip independent of the inclination, as found in a jet-driven bow shock model by Hartigan, Raymond, & Hartmann (1987). As a result, this model produces a similar velocity range as that seen in the W1 lobe.

The PV diagrams for model 4 are presented in Figure 17. The PV structures associated with the leading shock are similar to that seen in model 1. There are also structures associated with the internal shocks projected at a velocity higher than that of the leading shock, showing a series of increases in velocity. These PV diagrams are different

from that of the W1 lobe, which shows a single nonlinear increase in velocity with increasing distance. Hence, the bow-like structures seen in the W1 lobe may not be associated with internal shocks.

### 5.3. Line Ratios and Intensities

Here we compare the optical emission line fluxes derived from our simulations to the observations (Table 2). Since models 1 and 4 can produce a lobe with a collimation similar to that of the W1 lobe, we compare these in detail to the observations. The fluxes always peak at the tip of the lobe in both the simulations and observations. However, the ratios of the  $[\text{OI}]$  to  $[\text{SII}]$  peak fluxes derived from our simulations are too low compared to those derived from high resolution HST observations, indicating that the temperatures of the shocked AGB wind at the tip in our simulations ( $\sim 2 \times 10^4 \text{ K}$ ) are always much higher than observed ( $\sim 8 \times 10^3 \text{ K}$ ) (see Fig. 18). This conclusion is further supported by the groundbased observations. For example, the ratios of the  $[\text{OIII}]$  and  $[\text{NII}]$  total fluxes to the  $[\text{SII}]$  total fluxes in the tip of the lobe in the simulations are significantly higher than observed, which also indicates that the temperatures at the tip in the simulations are much higher than observed. Notice that in the observations, the  $[\text{OIII}]$  to  $[\text{SII}]$  ratio indicates a significantly higher temperature ( $\sim 30,000 \text{ K}$ ) than that indicated by the ratios of  $[\text{NII}]$  and  $[\text{OI}]$  to  $[\text{SII}]$  ( $\sim 15,000 \text{ K}$ ). Thus, the  $[\text{OIII}]$  emission comes from a region hotter than that of the  $[\text{NII}]$  and  $[\text{OI}]$  emission, consistent with an existence of a temperature stratification in the tip. Our models also show similar temperature stratification, although as mentioned above, the model temperatures are higher than observed.

The high temperatures at the tip of the shell in our simulations are produced by the dense and cold jet-like structure at the tip as it outruns the shell and shocks the AGB wind at the head before the shell does. The shell at the tip then interacts with the shocked AGB wind, resulting in a temperature higher than observed. The jet-like structure is formed as the shocked fast wind material flows toward the tip (Canto, Tenorio-Tagle, & Rozyczka 1988; Frank, Balick, & Livio 1996b). In reality, the cold dense jet-like material may mix with the hot shell material at the tip of the lobe (e.g., due to instabilities), significantly lowering the temperature there. Further simulations with high resolution are needed to test this idea. It is interesting to note that the observed line ratios at the tip of the W1 lobe (and thus the inferred temperature) are similar to those in the internal shocks in model 4. These internal shocks lack the jet-like structure at the tip in our simulations, thus supporting the idea that the jet-like structure is responsible for the high temperatures at the tip.

Although these models (1 and 4) produce a peak  $[\text{SII}]$  flux comparable to that of the observations, the total  $[\text{SII}]$  fluxes in our simulations are much less than observed because of the lack of significant emission within the body of the lobe. New simulations will need to address this discrepancy. Note that such simulations will also have to explain that the observed ratio of the  $[\text{OI}]$  to  $[\text{SII}]$  fluxes in the body of the lobe is smaller than that at the tip (which implies that the body of the lobe is hotter than the tip).

#### 5.4. The nature and origin of the collimated fast wind in CRL 618

The fast wind in CRL 618 is very unlikely to be a steady wind. This conclusion is most directly supported by the presence of the optical bow-like structures within the body of the lobe (see discussion in §5.1). Furthermore, CRL 618 is known to have a fast ( $\sim 200 \text{ km s}^{-1}$ ), compact (size  $\lesssim 5''$ ) bipolar molecular outflow (Neri et al. 1992). Only our pulsed wind model produces material moving at such high speeds close to the central source.

Since AGB winds are thought to be driven by radiation pressure on dust grains (see review by Habing 1996), we need to consider the possibility that the fast winds in PPNs are also powered by radiation pressure. In our models, the momentum flux per steradian of the fast wind is

$$\dot{P}_f = \frac{\dot{M}_f v_{fo}}{4\pi K} \exp[-3(\frac{\theta}{\theta_f})^2] \equiv \dot{P}_{fo} \exp[-3(\frac{\theta}{\theta_f})^2] \quad (17)$$

The luminosity of CRL 618 is  $L \sim 10^4 L_\odot$  (Goodrich 1991), giving a radiation momentum flux per steradian of  $\dot{P}_L = L/4\pi c \sim 10^{34} \text{ erg cm s}^{-1} \text{ yr}^{-1} \text{ sr}^{-1}$ . Thus,  $\dot{P}_f \gg \dot{P}_L$  within the opening angle of the CFW in our models (see Table 1), implying that the CFW can not be driven by radiation pressure. It is likely that the fast wind is launched by magneto-centrifugal forces from a magnetized accretion disk and star system (Blackman, Frank, & Welch 2001). The accretion disk may be formed in a binary system as the material flows from one star to another (Soker & Rapaport 2000). In this case, the gravitational binding energy in the accreting material is converted into the kinetic energy of the fast wind.

#### 5.5. Application to other PPN: OH 231.8+4.2

The simulation of model 2 may provide a clue to the formation of another PPN, OH 231.8+4.2. This PPN is bipolar, showing two strong and wide bow-like structures in H $\alpha$  at the tip of both the northern and southern lobes (Bujarrabal et al. 2002). A fast, collimated, dense CO structure is seen inside each lobe along the axis (Sánchez Contreras et al. 2000). Recently, it has been proposed that the two bow-like structures in both northern and southern lobes trace the forward and backward shocks driven by a dense jet (Bujarrabal et al. 2002). Models with an overdense cylindrical jet have difficulty producing as wide and strong bow-like emission for the backward shock as that for the forward shock due to the fast cooling of the backward shock (Raga et al. 1995). In contrast, a fast collimated wind can readily produce two strong and wide bow-like structures at the tip as those seen in model 2 (see Figure 15). Coincidentally, the collimation of the lobe and the velocities of both the forward and backward shocks in this model are similar to those derived by Bujarrabal et al. (2002) for the northern lobe of OH 231.8+4.2. As a result, if the two bow-like structures are to be associated with the forward and backward shocks, a tenuous collimated fast wind may be needed. If this is the case, the observed dense CO collimated structure would represent the dense core of a cool, latitudinally stratified fast wind. The lengths of the two lobes are different and may be due to an intrinsic difference in the velocity on each side of the bipolar fast wind (Soker 2002).

#### 6. SUMMARY AND CONCLUSIONS

We have presented a number of simulations of a collimated fast wind interacting with a spherical AGB wind. In our simulations, we have used a dense AGB wind with a high mass-loss rate typical of PPNs like CRL 618. The parameters of the fast wind are chosen to give a shell velocity at the tip of about  $150 \text{ km s}^{-1}$ , comparable to that seen in CRL 618. Under these assumptions, the main results from the simulations are the following:

1. The shell dynamics is determined by the velocity of the fast wind. For a  $300 \text{ km s}^{-1}$  fast wind, the cooling of the shocked fast wind is fast enough to remove the heat obtained from the fast wind, so that the shell is thin and momentum-driven. For a  $1000 \text{ km s}^{-1}$  fast wind, however, the shocked fast wind does not cool fast enough and expands sideways into a hot cocoon surrounding the fast wind. The fast wind itself becomes a ripple jet, so that the shell is essentially driven by a jet and its kinematics can be described by a ballistic bow shock model.
2. Although the AGB wind is spherical, the shell driven by a collimated fast wind has the shape of a highly collimated lobe. For a shell driven by a  $300 \text{ km s}^{-1}$  fast wind, the collimation of the shell increases roughly linearly with the decreasing opening angle of the fast wind. However, for a shell driven by a  $1000 \text{ km s}^{-1}$  fast wind, the collimation increases slowly with the decreasing opening angle.
3. A time-varying velocity of the fast wind produces a series of internal shock pairs interacting with the inner surface of the shell. Due to radial expansion of the fast wind, the density of the internal shocks decreases rapidly with distance.

We have also derived various emission diagnostics from our simulations. The main results are the following:

1. For a  $300 \text{ km s}^{-1}$  fast wind, the shell is composed of the shocked AGB wind (outer shell) and the shocked fast wind (inner shell). The optical emission arises mostly from the newly shocked AGB wind at the tip of the lobe, forming a bow-like structure. If the velocities of the shocked fast wind and the shocked AGB wind are similar, two bow-like structures are seen at the tip because the newly shocked fast wind also contributes significantly to the emission.
2. For a  $1000 \text{ km s}^{-1}$  fast wind, the shell is dominantly composed of the shocked AGB wind, and the optical emission again forms a bow-like structure at the tip. The shocked fast wind, however, forms a tenuous and hot, X-ray emitting structure interior to the shell.
3. When the velocity of the fast wind is time-varying, bow-shaped optical emission structures are seen associated with the internal shocks along the body of the lobe. This emission decreases rapidly away from the source.

4. The position-velocity (PV) diagrams from all our models show a broad range of velocities at the tip. However, the velocity range at the tip depends on the shell dynamics and the relative contributions of the shocked fast wind and the shocked AGB wind. For a momentum-driven shell, the velocity range depends on the inclination. For a shell driven by a ballistic bow shock, however, the velocity range is independent of the inclination and is equal to the shock velocity at the tip. When the velocity of the fast wind is time-variable, a series of increases in the velocity are seen in the PV diagrams.

Comparing our simulations to the observations of the PPN CRL 618, we find that

1. A  $300 \text{ km s}^{-1}$  collimated fast wind with an opening angle of  $10^\circ$  can readily produce a highly collimated lobe similar to the W1 lobe in this object. However, a  $1000 \text{ km s}^{-1}$  fast wind, even with an opening of  $5^\circ$ , has difficulty producing such a highly collimated lobe.
2. Our models can produce an optical bow-like structure at the tip similar to that seen in the W1 lobe. However, they have difficulty producing several additional bright optical bow-like structures seen in the body of the lobe. A fast wind with a less steep (than  $r^{-2}$ ) radial density gradient may help to remove this difficulty.
3. The PV diagrams derived from our simulations are qualitatively consistent with the observations.

However, the observed velocity range at the tip of the W1 lobe is larger than the momentum-driven shell model and may favor a shell driven by a ballistic bow shock.

4. The  $[\text{SII}]\lambda 6716\text{\AA}/\lambda 6730\text{\AA}$  ratios at the tip of the lobe in our simulations are all about 0.5 (implying an electron density of  $\sim 10^4 \text{ cm}^{-3}$ ), as observed.
5. Specific line ratios indicate that the temperatures at the tip of the lobe in our simulations are higher than observed. This may result from insufficient mixing of hot and cold material in the tip in our simulations. A comparison of the inferred temperatures from the  $[\text{OIII}]/[\text{SII}]$  ratio to that from the  $[\text{NII}]/[\text{SII}]$  and  $[\text{OI}]/[\text{SII}]$  ratios indicates a temperature stratification in the tip, both for the simulations and observations.
6. The collimated fast wind is unlikely to be steady and is not radiatively driven.

We thank Noam Soker, Vikram Dwarkadas and Garrelt Mellema for their comments about this paper. We thank C. Sánchez Contreras for fruitful conversations about the observations of CRL 618 as well as providing unpublished data on line ratios. This work was performed while C.-F. Lee held a National Research Council Research Associateship Award at the Jet Propulsion Laboratory, Caltech. R.S. acknowledges support by NASA through a Long Term Space Astrophysics grant (no. 399-20-61-00-00).

## APPENDIX

### EMISSION CALCULATION

The optical emission is assumed to be a thermal equilibrium (LTE) optically thin emission, so that the emissivity is given by

$$\epsilon = \frac{x f_i f_u n A_{ul} E_{ul}}{4\pi} \quad (\text{A1})$$

where  $x$ ,  $f_i$ ,  $f_u$ ,  $A_{ul}$ ,  $E_{ul}$  are the abundance of the element relative to hydrogen nuclei, ionization fraction of the ions, fraction of the ions in the upper excited state, Einstein A coefficient, and energy separation between the upper and lower excited states, respectively. The abundances relative to hydrogen nuclei are assumed to be  $4.17 \times 10^{-4}$ ,  $9.77 \times 10^{-6}$  and  $1.28 \times 10^{-4}$  for O, S and N, respectively. The ionization fractions of [OI] and [OIII] as a function of temperature are taken from Nahar (1999), [NII] from Nahar & Pradhan (1997) and [SII] from Shull & van Steenberg (1982).  $f_u$  is obtained by solving the level populations with the relevant atomic quantities taken from Mendoza (1983). The X-ray emission is also assumed to be an equilibrium optically thin emission. It is calculated with the Raymond & Smith (1977) model and a solar abundance from Anders & Grevesse (1989).

## REFERENCES

Anders, E. & Grevesse, N. 1989, *Geochim. Cosmochim. Acta*, 53, 197

Balick, B. & Frank, A. 2002, *ARA&A*, 40, 439

Balick, B., Preston, H. L., & Icke, V. 1987, *AJ*, 94, 1641.

Balick, B., Rutgers, M., Terzian, Y., & Chengalur, J. N. 1993, *ApJ*, 411, 778.

Biro, S. and Raga, A. C. 1994, *ApJ*, 434, 221

Blackman, E. G., Frank, A., & Welch, C. 2001, *ApJ*, 546, 288

Blandford, R. D. & Payne, D. G. 1982, *MNRAS*, 199, 883

Blondin, J. M. & Lundqvist, P. 1993, *ApJ*, 405, 337.

Blondin, J. M., Fryxell, B. A. & Konigl, A. 1990, *ApJ*, 360, 370

Borkowski, K. J., Blondin, J. M., & Harrington, J. P. 1997, *ApJ*, 482, L97.

Bujarrabal, V. & Alcolea, J. 1991, *A&A*, 251, 536

Bujarrabal, V., Castro-Carrizo, A., Alcolea, J., & Sánchez Contreras, C. 2001, *A&A*, 377, 868

Bujarrabal, V., Alcolea, J., Sánchez Contreras, C., & Sahai, R. 2002, *A&A*, 389, 271

Canto, J., Tenorio-Tagle, G., & Rozyczka, M. 1988, *A&A*, 192, 287.

Chevalier, R. A. & Luo, D. 1994, *ApJ*, 421, 225

Chu, Y., Jacoby, G. H., & Arendt, R. 1987, *ApJS*, 64, 529

Cliffe, J. A., Frank, A., Livio, M., & Jones, T. W. 1995, *ApJ*, 447, L49

Corradi, R. L. M. & Schwarz, H. E. 1995, *A&A*, 293, 871

Dalgarno, A. & McCray, R. A. 1972, *ARA&A*, 10, 375 *MNRAS*, 314, 241

Dwarkadas, V. V. & Balick, B. 1998, *ApJ*, 497, 267.

Dwarkadas, V. V., Chevalier, R. A., & Blondin, J. M. 1996, *ApJ*, 457, 773.

Dyson, J. E. & Williams, D. A. 1980, *The Physics of the Interstellar Medium* (New York: Wiley)

Frank, A. 1999, *New Astronomy Review*, 43, 31

Frank, A. & Mellema, G. 1994, *ApJ*, 430, 800.

Frank, A. & Mellema, G. 1996, *ApJ*, 472, 684

Frank, A., Balick, B., & Livio, M. 1996, *ApJ*, 471, L53.

Frank, A., Ryu, D., & Davidson, K. 1998, *ApJ*, 500, 291

Garcia-Segura, G. 1997, *ApJ*, 489, L189

Gardiner, T. A. & Frank, A. 2001, *ApJ*, 557, 250

Goodrich, R. W. 1991, *ApJ*, 376, 654

Guerrero, M. J., Chu, Y., & Gruendl, R. A. 2000, *ApJS*, 129, 295

Habing, H. J. 1996, *A&A Rev.*, 7, 97

Hartigan, P., Raymond, J., & Hartmann, L. 1987, *ApJ*, 316, 323

Hartmann, L. & Kenyon, S. J. 1996, *ARA&A*, 34, 207 889

Icke, V., Balick, B., & Frank, A. 1992, *A&A*, 253, 224.

Kahn, F. D. 1983, *IAU Symp. 103: Planetary Nebulae*, 103, 305.

Knapp, G. R. & Morris, M. 1985, *ApJ*, 292, 640

Konigl, A. & Pudritz, R. E. 2000, *Protostars and Planets IV*, 759

Kwok, S., Purton, C. R., & Fitzgerald, P. M. 1978, *ApJ*, 219, L125.

Kwok, S., Su, K. Y. L., & Hrivnak, B. J. 1998, *ApJ*, 501, L117.

Lee, C., Stone, J. M., Ostriker, E. C., & Mundy, L. G. 2001, *ApJ*, 557, 429.

MacDonald, J. & Bailey, M. E. 1981, *MNRAS*, 197, 995

Mellema, G. 1995, *MNRAS*, 277, 173.

Mendoza, C. 1983, *IAU Symp. 103: Planetary Nebulae*, 103, 143.

Nahar, S. N. 1999, *ApJS*, 120, 131.

Nahar, S. N. & Pradhan, A. K. 1997, *ApJS*, 111, 339.

Neri, R., García-Burillo, S., Guelin, M., Cernicharo, J., Guilloteau, S., & Lucas, R. 1992, *A&A*, 262, 544

Neri, R., Kahane, C., Lucas, R., Bujarrabal, V., & Loup, C. 1998, *A&AS*, 130, 1.

Ostriker, E. C., Lee, C., Stone, J. M., & Mundy, L. G. 2001, *ApJ*, 557, 443.

Raga, A. C. & Cabrit, S. 1993, *A&A*, 278, 267

Raga, A. C., Taylor, S. D., Cabrit, S., & Biro, S. 1995, *A&A*, 296, 833

Raymond, J. C. & Smith, B. W. 1977, *ApJS*, 35, 419

Rozyczka, M. & Franco, J. 1996, *ApJ*, 469, L127

Sahai, R. 2001, *Post-AGB Objects as a Phase of Stellar Evolution*, 53.

Sahai, R. 2003, *IAU*, in press

Sahai, R. & Trauger, J. T. 1998, *AJ*, 116, 1357

Sahai, R. et al. 1998, *ApJ*, 493, 301.

Sánchez Contreras, C. & Sahai, R. 2001, *ApJ*, 553, L173.

Sánchez Contreras, C., & Sahai, R. & Gil De Paz, A 2002, *ApJ*, in press

Sánchez Contreras, C., Bujarrabal, V., Miranda, L. F., & Fernández-Figueredo, M. J. 2000, *A&A*, 355, 1103

Schwarz, H. E., Aspin, C., Corradi, R. L. M., & Reipurth, B. 1997, *A&A*, 319, 267

Shu, F., Najita, J., Ostriker, E., Wilkin, F., Ruden, S., & Lizano, S. 1994, *ApJ*, 429, 781

Shull, J. M. & van Steenberg, M. 1982, *ApJS*, 48, 95.

Soker, N. 2002, *ApJ*, 568, 726

Soker, N. & Rappaport, S. 2000, *ApJ*, 538, 241

Steffen, W. & López, J. A. 1998, *ApJ*, 508, 696

Stone, J. M. & Norman, M. L. 1993, *ApJ*, 413, 210

Stone, J. M. & Norman, M. L. 1994, *ApJ*, 420, 237

Su, K. Y. L., Volk, K., Kwok, S., & Hrivnak, B. J. 1998, *ApJ*, 508, 744.

Suttner, G., Smith, M. D., Yorke, H. W. & Zinnecker, H. 1997, *A&A*, 318, 595

Trammell, S. R. 2000, *ASP Conf. Ser. 199: Asymmetrical Planetary Nebulae II: From Origins to Microstructures*, 147.

TABLE 1  
PARAMETERS FOR FAST WINDS

Model	$\dot{M}_f$ ( $10^{-7} M_{\odot} \text{ yr}^{-1}$ )	$v_{fo}$ (100 km s $^{-1}$ )	$\theta_f^a$ (degree)	$R^b$ ( $10^{-3}$ )	$K$ (%)	$\dot{P}_{fo}/\dot{P}_L^c$
1	25	3	10	7.6	86.5	158
2	100	3	20	30.2	39.6	158
3	2.5	10	10	7.6	86.5	53
4*	25	3	10	7.6	86.5	158

<sup>a</sup>Opening angle

<sup>b</sup>Total mass-loss rate within 10° from the pole/Total mass-loss rate

<sup>c</sup>Momentum flux per steradian of the fast wind at the pole/Radiation momentum flux per steradian

\*Model 4 is Model 1 with time variation in the density and velocity.

TABLE 2  
EMISSION LINE DIAGNOSTICS

	Peak Intensity				Observations <sup>a</sup>	
	Model					
	1	2	3	4		
[OI] $\lambda 6300\text{\AA}^c$	0.5	0.9	1.3	0.53	5.4	
[SII] $\lambda\lambda 6730, 6716\text{\AA}^b$	1.1e-13	6.1e-13	1.1e-12	8.1e-14	1.4e-13	
[NII] $\lambda 6583\text{\AA}^c$	5.0	6.8	9.3	3.6	—	
[OIII] $\lambda 5007\text{\AA}^c$	5.6	7.5	19.7	90	—	
Total Flux in the Peak <sup>d</sup>						
	Model				Observations <sup>e</sup>	
	1	2	3	4		
	0.6	0.8	0.8	0.7	1.5	
[OI] $\lambda 6300\text{\AA}^g$	6.6e-15	3.2e-13	3.7e-13	5.1e-15	1.1e-14	
[SII] $\lambda\lambda 6730, 6716\text{\AA}^f$	3.9	5.0	6.5	2.0	1.3	
[OIII] $\lambda 5007\text{\AA}^g$	2.1	3.2	9.8	0.7	0.07	

<sup>a</sup>Adopted from the HST images in Sahai et al. (2003)

<sup>b</sup>Peak Intensity in unit of erg s $^{-1}$  cm $^{-2}$  arcsec $^{-2}$ .

<sup>c</sup>Peak Intensity normalized to that of [SII] $\lambda\lambda 6730, 6716\text{\AA}$

<sup>d</sup>Measured in a 2"  $\times$  2" box covering the tip of the W1 lobe.

<sup>e</sup>From groundbased observations (SCSG02 and priv. comm.)

<sup>f</sup>Total flux in the peak in unit of erg s $^{-1}$  cm $^{-2}$ .

<sup>g</sup>Total flux in the peak normalized to that of [SII] $\lambda\lambda 6730, 6716\text{\AA}$

FIG. 1.— Simulation of model 1 as the fast wind propagates to a distance of  $\sim 10^{17}$  cm, a length similar to that of the lobes in CRL 618. The age of the fast wind is 177 years. In this model,  $\dot{M}_f = 2.5 \times 10^{-6} M_{\odot} \text{ yr}^{-1}$ ,  $v_{fo} = 300 \text{ km s}^{-1}$ , and  $\theta_f = 10^\circ$ . (a) shows the contours of the fast wind tracer,  $c$ , superposed on the density distribution. Contours are 0.1, 0.5 and 0.9. The dashed line is the shell structure derived from the momentum-driven shell model with Equation 10. (b) and (c) show the contours of  $c_w$  and  $c_a$ , respectively, superposed on the density distribution.  $c_a$  and  $c_w$  trace respectively the flows of the AGB wind and the fast wind emanating within the angular segment  $5^\circ < \theta < 7.5^\circ$ . Contours are 0.1, 0.5 and 0.9. (d) shows the velocity distribution superposed on the pressure distribution. (e) shows the temperature distribution. The gray-scale wedges along the right side indicate the values for the gray-scale images. (A), (B) and (C) show respectively the blow-ups for the regions in the boxes A, B and C. Regions i, ii, iii, iv and v indicate unshocked fast wind, shocked fast wind, mixture of shocked fast and AGB winds, shocked AGB wind and unshocked AGB wind, respectively. Contact discontinuity is located in region iii.

FIG. 2.— Transverse velocity ( $v_R$ ) and longitudinal velocity ( $v_z$ ) of the shell material for model 1 at 177 years. The gray-scale indicates the mass column density on a linear stretch. The solid lines indicate the  $R$  and  $z$  components of the mean shell velocity obtained from the simulation. The dashed lines indicate the  $R$  and  $z$  components of the velocity of the newly shocked fast wind derived from Equation 11.

FIG. 3.— Coordinate system used for the shell dynamics. The thick line indicates the shell.  $v_f$ ,  $v_s$  and  $r_s$  are the velocity of the fast wind, the shell velocity and the shell radius, respectively.  $\alpha$  is the angle between the shell normal and the shell velocity.

FIG. 4.— Simulation of model 2. The age is 188 years. In this model,  $\dot{M}_f = 1 \times 10^{-5} M_{\odot} \text{ yr}^{-1}$ ,  $v_{fo} = 300 \text{ km s}^{-1}$ , and  $\theta_f = 20^\circ$ . The captions are the same as Figure 1.

FIG. 5.— Simulation of model 3. The age is 180 years. In this model,  $\dot{M}_f = 2.5 \times 10^{-7} M_{\odot} \text{ yr}^{-1}$ ,  $v_{fo} = 1000 \text{ km s}^{-1}$ , and  $\theta_f = 10^\circ$ . The captions are the same as Figure 1, except that the dashed line in (a) is the shell structure derived from the ballistic bow shock model given by Ostriker et al. (2001).

FIG. 6.— Transverse velocity ( $v_R$ ) and longitudinal velocity ( $v_z$ ) of the shell material for model 3 at 180 years. As in Fig. 2, the gray-scale indicates the mass column density on a linear stretch. The solid lines indicate the  $R$  and  $z$  components of the mean shell velocity, while the dashed lines indicate the  $R$  and  $z$  components of the immediate postshock velocity of the AGB wind derived from the ballistic bow shock model.

FIG. 7.— Simulation of model 4. The age is 166 years. In this model, the fast wind has the same parameters as that in model 1 but has a time-variation with  $A = 0.5$  and  $P = 22$  years (see Equation 5). The captions are the same as Figure 1, except that the dashed lines in (a) are derived from Equation 13.

FIG. 8.— HST images of CRL 618 in [OI] and [SII] emission (logarithmic stretch). The cross indicates the approximate position of the central source. The gray-scale wedges along the right side indicate the values for the gray-scale images. The intensity of the image has a unit of  $\text{erg s}^{-1} \text{ cm}^{-2} \text{ arcsec}^2$ .

FIG. 9.— Integrated optical emission and line ratio of  $[\text{SII}]\lambda 6716\text{\AA}/\lambda 6730\text{\AA}$  for model 1 at an inclination of  $i=30^\circ$ . The optical emission is in logarithmic scale with an angular resolution similar to that of HST images. The gray-scale wedges along the right side indicate the values for the gray-scale images.

FIG. 10.— Same as that in Figure 9 except for model 2.

FIG. 11.— Same as that in Figure 9 except for model 3.

FIG. 12.— Integrated X-ray emission and spectrum for model 3 in the 0.2-1.5 keV energy range at an angular resolution of 0.5" and an energy resolution of 50 eV. The gray-scale wedge along the right side indicates the values for the gray-scale image. In the spectrum, there are strong emission lines from oxygen at about 570 and 653 eV, and from iron at about 730 and 826 eV.

FIG. 13.— Same as that in Figure 9 except for model 4.

FIG. 14.— Position-velocity diagrams of the [OI] emission for model 1 at an inclination of  $i=30^\circ$ . PV diagram on the left has an angular resolution of 0.05" and a velocity resolution of  $10 \text{ km s}^{-1}$ . PV diagram on the right is degraded to an angular resolution of 1" and a velocity resolution of  $50 \text{ km s}^{-1}$  for comparing with current groundbased observations.

FIG. 15.— Same as that in Figure 14 except for model 2.

FIG. 16.— Same as that in Figure 14 except for model 3.

FIG. 17.— Same as that in Figure 14 except for model 4.

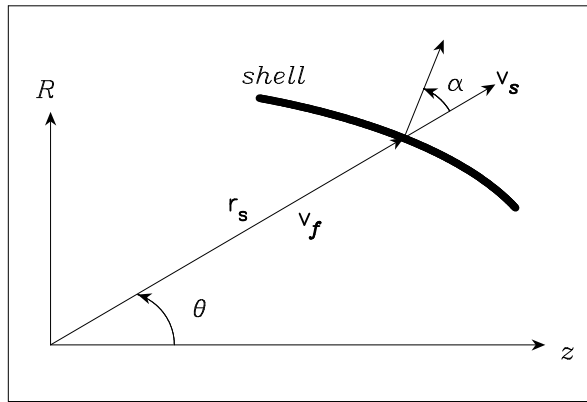
FIG. 18.— Line ratios of the  $[\text{OI}]\lambda 6300\text{\AA}$ ,  $[\text{NII}]\lambda 6583\text{\AA}$  and  $[\text{OIII}]\lambda 5007\text{\AA}$  emission to the  $[\text{SII}]\lambda\lambda 6730, 6716\text{\AA}$  emission. Solid lines are for number density =  $2 \times 10^3 \text{ cm}^{-3}$ , dashed lines for  $10^4 \text{ cm}^{-3}$ , and dotted-dashed lines for  $5 \times 10^4 \text{ cm}^{-3}$ . The line ratios are derived assuming equilibrium optically thin emission (see Appendix).

This figure "fig1.jpg" is available in "jpg" format from:

<http://arxiv.org/ps/astro-ph/0211510v1>

This figure "fig2.jpg" is available in "jpg" format from:

<http://arxiv.org/ps/astro-ph/0211510v1>



This figure "fig4.jpg" is available in "jpg" format from:

<http://arxiv.org/ps/astro-ph/0211510v1>

This figure "fig5.jpg" is available in "jpg" format from:

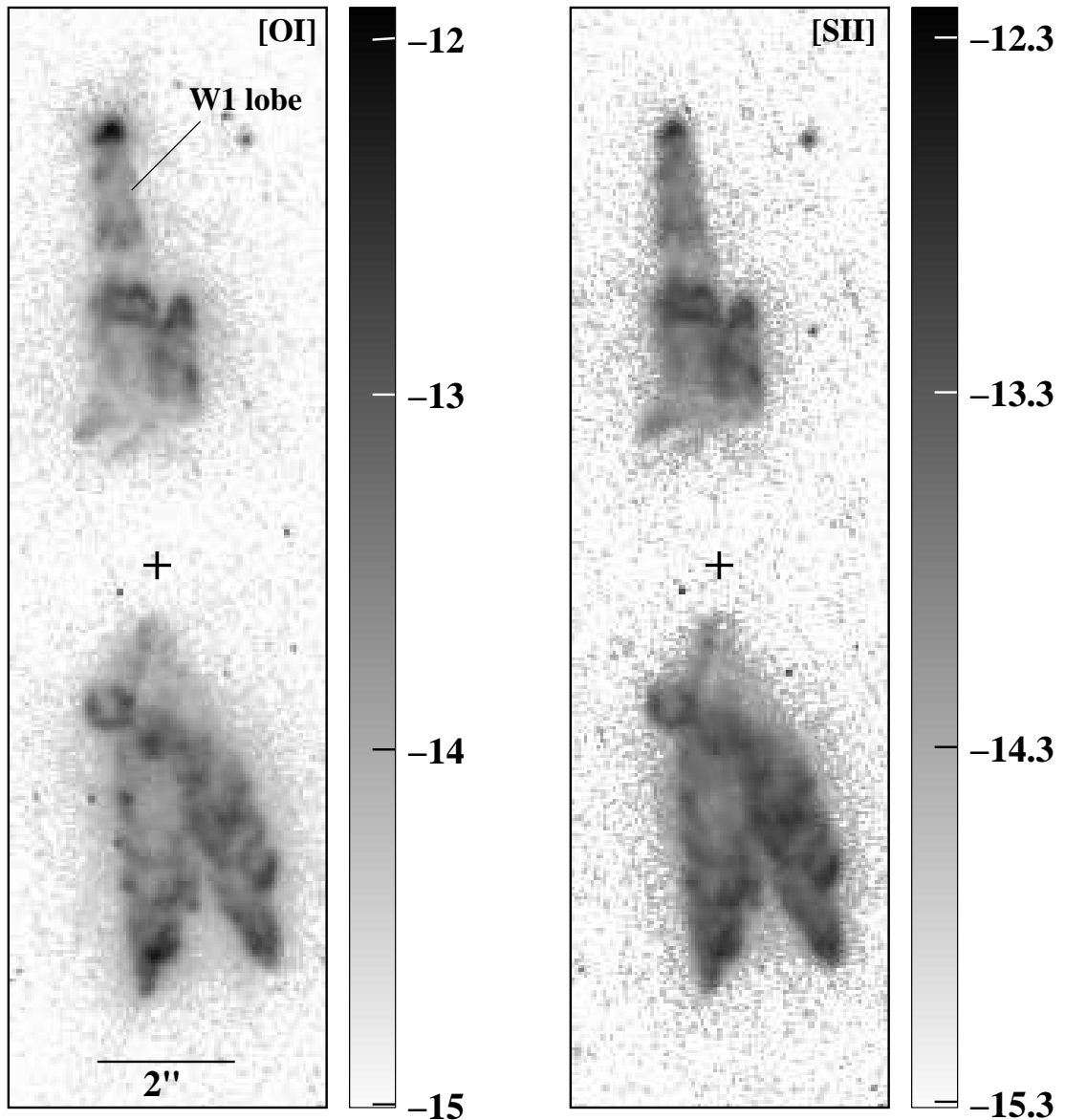
<http://arxiv.org/ps/astro-ph/0211510v1>

This figure "fig6.jpg" is available in "jpg" format from:

<http://arxiv.org/ps/astro-ph/0211510v1>

This figure "fig7.jpg" is available in "jpg" format from:

<http://arxiv.org/ps/astro-ph/0211510v1>



This figure "fig9.jpg" is available in "jpg" format from:

<http://arxiv.org/ps/astro-ph/0211510v1>

This figure "fig10.jpg" is available in "jpg" format from:

<http://arxiv.org/ps/astro-ph/0211510v1>

This figure "fig11.jpg" is available in "jpg" format from:

<http://arxiv.org/ps/astro-ph/0211510v1>

This figure "fig12.jpg" is available in "jpg" format from:

<http://arxiv.org/ps/astro-ph/0211510v1>

This figure "fig13.jpg" is available in "jpg" format from:

<http://arxiv.org/ps/astro-ph/0211510v1>

This figure "fig14.jpg" is available in "jpg" format from:

<http://arxiv.org/ps/astro-ph/0211510v1>

This figure "fig15.jpg" is available in "jpg" format from:

<http://arxiv.org/ps/astro-ph/0211510v1>

This figure "fig16.jpg" is available in "jpg" format from:

<http://arxiv.org/ps/astro-ph/0211510v1>

This figure "fig17.jpg" is available in "jpg" format from:

<http://arxiv.org/ps/astro-ph/0211510v1>

